ChemComm

ROYAL SOCIETY OF CHEMISTRY

COMMUNICATION

View Article Online
View Journal | View Issue

Cite this: *Chem. Commun.*, 2025, **61**, 16985

Received 31st July 2025,
Accepted 26th September 2025

DOI: 10.1039/d5cc04360c

rsc.li/chemcomm

# Pt nanoparticle-embedded NiFe-LDH nanoflowers as a high-performance cathode for rechargeable aqueous zinc–air batteries

Meilin Nie,[ab] Dapeng Liu,*[ab] Zerui Fu,[ab] Xianhang Li[b] and Yu Zhang *[ab]

**Rechargeable aqueous Zn–air batteries (ZABs) are promising due to their high energy density (1370 Wh kg$^{-1}$), safety, and environmental friendliness, but their development is hindered by slow oxygen redox kinetics. Herein, we have synthesized Pt nanoparticle-embedded NiFe layered double hydroxide (Pt/NiFe-LDH) nanoflowers *via* an *in situ* reduction method. As a cathode, Pt/NiFe-LDH can exhibit remarkable bifunctional activity with an impressive $\Delta E$ value of 0.631 V, which achieves a half-wave potential of 0.861 V for the oxygen reduction reaction and a low overpotential of 262 mV at 10 mA cm$^{-2}$ for the oxygen evolution reaction, surpassing commercial Pt/C and $RuO_2$ benchmarks. When deployed in ZABs, the Pt/NiFe-LDH cathode delivers remarkable cycling stability over 1300 h.**

The urgent requirement to alleviate the energy crisis is intensifying the demand for sustainable, large-capacity electrochemical energy storage and conversion devices.[1–4] Rechargeable aqueous zinc–air batteries (ZABs) have been emerging as one of the most promising candidates due to their high theoretical energy density of 1370 Wh kg$^{-1}$, as well as good safety and environmental friendliness.[5] Typically, aqueous ZABs operate based on the reaction of Zn + $O_2$ ↔ ZnO, in which the air cathode plays the pivotal role during the discharge and charge processes.[6] Unfortunately, the sluggish oxygen reduction reaction (ORR)/oxygen evolution reaction (OER) kinetics of the cathode result in inferior battery performance.[7] The commercial noble metal-based cathode electrocatalysts such as Pt/C, $RuO_2$, and $IrO_2$ are currently considered as an ideal benchmark to improve the ORR/OER kinetics,[8] but their widespread application in ZABs is severely constrained by high cost and poor operational stability.[9] To address these issues, the design of electrocatalysts is of great necessity to deliver high utilization of noble metals, catalytic activity, and stability.[10]

Among noble metals, Pt has been identified as one of the most efficient catalysts for the ORR rather than the OER.[11] However, Pt nanoparticles tend to agglomerate, causing severe deterioration of catalytic activity.[12] In general, an appropriate catalyst support is quite needed to disperse Pt so as to improve its catalytic properties and utilization.[13] NiFe layered double hydroxide (NiFe-LDH) can serve as a good carrier to support noble metals due to three advantages: (1) their unique layered structures could provide a large surface area and abundant active sites,[14] (2) the abundant surface hydroxyl groups and interlayer multivalent anions to stabilize and uniform Pt,[15] and (3) they are stable towards alkaline electrolytes. Consequently, if the Pt/NiFe-LDH hybrid was formed, Pt could deliver superior ORR performance while NiFe-LDH showed good OER activity.

In this work, we have tried to synthesize Pt/NiFe-LDH hybrids *via* an *in situ* reduction method. This approach leverages NiFe-LDH as a carrier to uniformly disperse Pt nanoparticles while synergistically integrating their catalytic functions. The design is based on Fermi level alignment; due to the higher Fermi level of NiFe-LDH compared to Pt, electrons transfer from NiFe-LDH to Pt, resulting in charge redistribution which enables efficient bifunctional oxygen electrocatalysis.[16] The as-prepared Pt/NiFe-LDH has exhibited superior bifunctional performance, which achieves a low $\Delta E$ of 0.631 V with a positive half-wave potential ($E_{1/2}$) of 0.861 V *versus* RHE for the ORR and a low overpotential of 262 mV at 10 mA cm$^{-2}$ for the OER, surpassing commercial Pt/C and $RuO_2$. Furthermore, Pt/NiFe-LDH-based ZABs exhibit excellent cycling stability at 2 mA cm$^{-2}$ for over 1300 h. This work provides us with a new avenue for rationally designing and synthesizing efficient oxygen electrocatalysts toward practical implementation for energy storage and conversion systems.

A schematic illustration of the synthesis of Pt/NiFe-LDH is depicted in Fig. 1. Firstly, the NiFe-LDH nanoflowers were synthesized *via* a hydrothermal process. After that, $H_2PtCl_6$ was introduced into the LDH precursor solution under continuous stirring to ensure its homogeneous dispersion and the following adsorption of $H_2PtCl_6$ onto LDH. An instantaneous color change of the solution could be clearly observed from deep yellow to black (Fig. S1), indicating the reduction of $H_2PtCl_6$ into Pt nanoparticles by $NaBH_4$. Ultimately, Pt nanoparticles were

---

[a] *Hangzhou International Innovation Institute, Beihang University, Hangzhou 311115, P. R. China. E-mail: liudp@buaa.edu.cn, jade@buaa.edu.cn*
[b] *School of Chemistry, Beihang University, Beijing 100191, P. R. China*

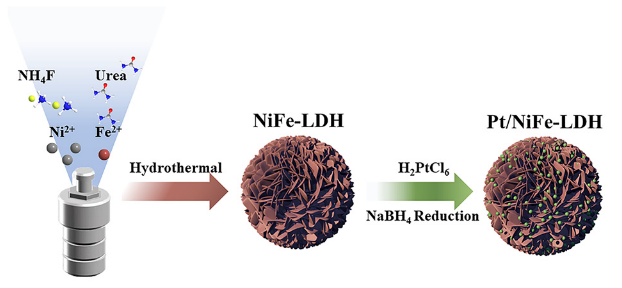

Fig. 1 Schematic illustration for the synthetic process of Pt/NiFe-LDH.

uniformly loaded on the nanoflowers, and the Pt, Ni, and Fe loadings in Pt/NiFe-LDH were determined to be approximately 13.8, 33.7, and 14.9 wt%, respectively, *via* inductively coupled plasma optical emission spectrometry (ICP-OES) as shown in Table S1.

Scanning electron microscopy (SEM) reveals NiFe-LDH's nanoflower morphology with interwoven nanosheets (Fig. 2a and Fig. S2a), providing abundant active sites. Pt deposition preserves this framework (Fig. 2b and Fig. S2b). Transmission electron microscopy (TEM) and high-resolution transmission electron microscopy (HRTEM) techniques confirm ultrafine Pt nanoparticles uniformly anchored on nanosheets (Fig. 2c), with 0.226 nm lattice fringes attributed to the (111) plane of Pt (Fig. 2d and Fig. S3). The average diameter of the Pt nanoparticles was calculated to be about 8 nm, with a narrow size distribution (Fig. S4). The high-angle annular dark-field scanning transmission electron microscopy (HAADF-STEM) image and the corresponding energy dispersive spectroscopy (EDS) mapping images (Fig. 2e and f) verify the homogeneous distribution of Fe, Ni, and Pt, confirming successful reduction.

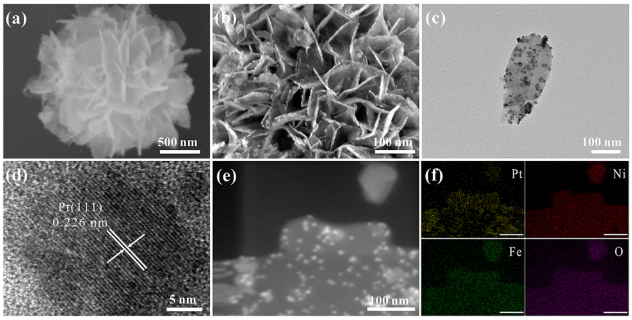

Fig. 2 Morphological characterization of NiFe-LDH and Pt/NiFe-LDH. SEM images of (a) NiFe-LDH and (b) Pt/NiFe-LDH; (c) TEM image of Pt/NiFe-LDH; (d) HRTEM image of Pt/NiFe-LDH; (e) HAADF-STEM image of Pt/NiFe-LDH; and (f) element mapping images of Pt/NiFe-LDH.

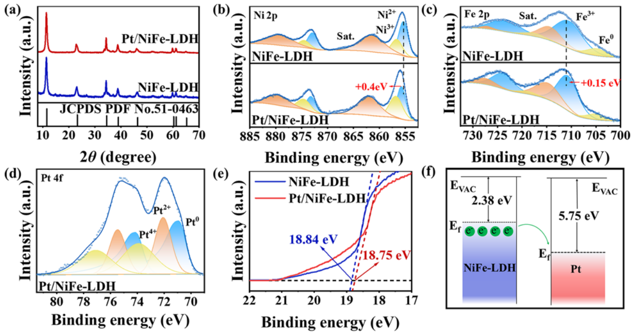

Fig. 3 Structural characterization of NiFe-LDH and Pt/NiFe-LDH. (a) XRD patterns of NiFe-LDH and Pt/NiFe-LDH; XPS spectra of (b) Ni 2p, (c) Fe 2p and (d) Pt 4f in NiFe-LDH and Pt/NiFe-LDH; (e) UPS spectra of NiFe-LDH and Pt/NiFe-LDH; and (f) schematic diagram of electron transfer.

The crystal structure and surface chemical states of the NiFe layered double hydroxide and Pt/NiFe-LDH were characterized. X-ray diffraction (XRD) patterns (Fig. 3a) confirm that both materials maintain the NiFe-LDH structure (JCPDS 51-0463), with characteristic (003) and (006) peaks at 11.5° and 23.3°. In comparison with NiFe-LDH, all the diffraction peaks of Pt/NiFe-LDH show no significant shift and no obvious Pt-related signal can be identified, indicating that the loading of Pt nanoparticles does not change the crystal structure of LDH. X-ray photoelectron spectroscopy (XPS) analysis reveals Ni, Fe, O (Fig. 3b, c and Fig. S5), and Pt (Fig. 3d) in Pt/NiFe-LDH. The Ni 2p spectrum shows Ni$^{2+}$ (2p$_{3/2}$ at 855.4 eV, 2p$_{1/2}$ at 872.9 eV) and Ni$^{3+}$ (2p$_{3/2}$ at 856.7 eV, 2p$_{1/2}$ at 874.5 eV) species, with Pt/NiFe-LDH exhibiting a 0.4 eV higher Ni 2p$_{3/2}$ binding energy and increased Ni$^{3+}$ content *versus* NiFe-LDH. The Fe 2p spectrum of NiFe-LDH can be separated into peaks attributed to Fe$^{3+}$ (2p$_{3/2}$ at 710.5 eV and 2p$_{1/2}$ at 723.3 eV), proving the existence of oxidized Fe in NiFe-LDH. And the Fe$^{3+}$ peaks reveal a positive shift of 0.15 eV in Pt/NiFe-LDH, which should be caused by the incorporation of Pt as well. Pt 4f spectra display metallic Pt$^{0}$ (4f$_{7/2}$ at 70.1 eV and 4f$_{5/2}$ at 74.1 eV), Pt$^{2+}$ (4f$_{7/2}$ at 72.0 eV and 4f$_{5/2}$ at 75.5 eV), and Pt$^{4+}$ (4f$_{7/2}$ at 73.9 eV and 4f$_{5/2}$ at 77.1 eV), confirming Pt reduction. Overall, the XPS spectra in Pt/NiFe-LDH compared with NiFe-LDH indicate that Ni and Fe are oxidized after the incorporation of Pt, owing to electron transfer from Ni and Fe to Pt.[17] Ultraviolet photoelectron spectroscopy (UPS) measurements determine work functions ($\Phi$) of 2.38 eV (NiFe-LDH) and 2.47 eV (Pt/NiFe-LDH).[18] And the work function of Pt/NiFe-LDH is found to be between that of Pt (5.75 eV)[19] and NiFe-LDH. Consequently, after the formation of the hybrid, electrons could spontaneously transfer from NiFe-LDH to Pt (Fig. 3f), consistent with the XPS results. The modified electron distribution effectively optimizes the catalytic activity of NiFe-LDH.[16]

We evaluated the oxygen reduction reaction (ORR) performance of Pt/NiFe-LDH using rotating disk electrode (RDE) measurements. Samples with different H$_2$PtCl$_6$ and NiFe-LDH mixing durations (2 h, 12 h, 24 h) reveal that the prolonged mixing time is associated with enhanced ORR activity (Fig. S6a and b), evidenced by positive shifts in half-wave potential ($E_{1/2}$) and reduced Tafel slopes. The sample with 24 h mixing time, which shows the best catalyst activity in the samples, was chosen for further tests. Pt/NiFe-LDH exhibits superior activity with $E_{1/2}$ = 0.861 V *vs.* reversible hydrogen electrode (RHE), outperforming commercial Pt/C (0.828 V), and comparable limiting current density (5.07 mA cm$^{-2}$ vs Pt/C's 5.57 mA cm$^{-2}$) (Fig. 4a). Pt/NiFe-LDH shows faster ORR kinetics (Tafel slope = 69.11 mV dec$^{-1}$ *vs.* Pt/C's 72.49 mV dec$^{-1}$) (Fig. S7a). For the oxygen evolution

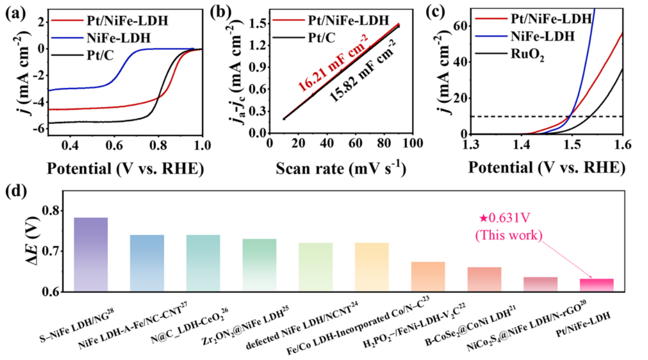

**Fig. 4** The electrocatalytic activities of Pt/NiFe-LDH, NiFe-LDH, Pt/C, and $RuO_2$. (a) LSV ORR curves in $O_2$ saturated 0.1 M KOH at 1600 rpm; (b) LSV OER curves in 1 M KOH at 1600 rpm; (c) half-value current density difference at 1.12 V *vs.* RHE with scanning rate; (d) comparison of the performance of various electrocatalysts.[20–28]

reaction (OER) (Fig. 4b), Pt/NiFe-LDH achieves an overpotential of 262 mV at 10 mA cm$^{-2}$ (1.492 V *vs.* RHE), surpassing NiFe-LDH (1.494 V) and $RuO_2$ (1.536 V), with favorable kinetics (Tafel slope = 27.71 mV dec$^{-1}$ *vs.* $RuO_2$'s 51.67 mV dec$^{-1}$) (Fig. S7b). Optimized electron transfer between NiFe-LDH and Pt enhances efficient bifunctional oxygen electrocatalysis. Mixing time minimally affects OER performance (Fig. S6c and d), confirming that Pt incorporation preserves LDH's OER active structure while enabling bifunctionality. Electrochemical double-layer capacitance measurements reveal Pt/NiFe-LDH's higher double-layer capacitance (16.21 mF cm$^{-2}$ *vs.* Pt/C's 15.82 mF cm$^{-2}$), indicating greater active site exposure (Fig. 4c). Fig. 4d shows the comparison of the performance of various electrocatalysts.

ZABs employing Pt/NiFe-LDH as the air electrode catalyst were fabricated (Fig. 5a), with comparative systems using NiFe-LDH and Pt/C + $RuO_2$. The Pt/NiFe-LDH-based ZAB achieves an open-circuit potential of 1.44 V, surpassing NiFe-LDH (1.36 V) and approaching Pt/C + $RuO_2$ (1.47 V) (Fig. S8). At current densities of 2–10 mA cm$^{-2}$, Pt/NiFe-LDH exhibits discharge plateaus comparable to Pt/C + $RuO_2$ and superior to NiFe-LDH (Fig. S9), demonstrating excellent rate capability and reversibility. The specific capacity reaches 769.1 mAh g$^{-1}$ at 2 mA cm$^{-2}$, exceeding that of both Pt/C + $RuO_2$ (765.9 mAh g$^{-1}$) and NiFe-LDH (750.8 mAh g$^{-1}$) (Fig. 5b). Power density outperforms that of Pt/C + $RuO_2$ and NiFe-LDH (Fig. S10). Electrochemical impedance spectroscopy (Fig. S11) shows that the Pt/NiFe LDH catalyst exhibits a significantly lower charge transfer resistance when compared to NiFe LDH catalysts. As an exemplification for practical applications, a little fan can be powered by the Pt/NiFe-LDH-based ZAB. Remarkably, the Pt/NiFe-LDH-based ZAB maintains stable cycling for 1300 h at 2 mA cm$^{-2}$ with only a 4.2% energy efficiency loss (62.8% to 58.6%), while Pt/C + $RuO_2$ fails after 40 h and NiFe-LDH after 380 h (Fig. 5c). These results confirm Pt/NiFe-LDH as a superior bifunctional catalyst enabling ZABs with exceptional capacity, power density, and durability.

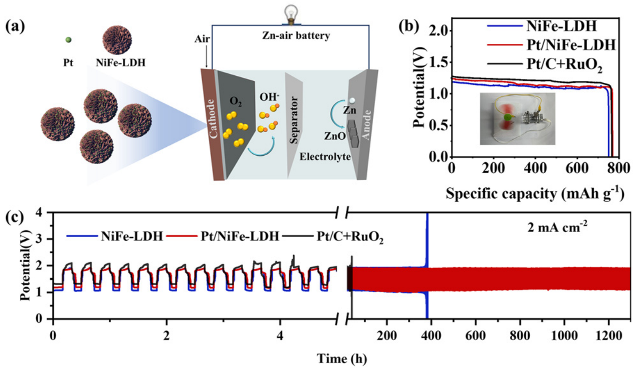

**Fig. 5** Performance of the assembled rechargeable ZABs with Pt/NiFe-LDH, NiFe-LDH and Pt/C + $RuO_2$ catalysts. (a) Schematic diagram of zinc-air battery; (b) discharge curves at 2 mA cm$^{-2}$; (c) long-term cycling performance of ZABs.

In summary, we successfully synthesise Pt nanoparticles loaded on NiFe-LDH nanosheets as a high-performance bifunctional electrocatalyst for rechargeable ZABs. The hybrid catalyst takes advantage of the synergistic interaction between the excellent ORR activity of Pt and the inherent OER ability of NiFe-LDH. The Pt/NiFe-LDH achieves an ORR $E_{1/2}$ of 0.861 V and an OER overpotential of 262 mV at 10 mA cm$^{-2}$, which outperforms Pt/C and $RuO_2$ and presents a $\Delta E$ of 0.631 V. ZABs employing Pt/NiFe-LDH demonstrate exceptional cycling stability (1300 h), initial energy efficiency (62.8%), and power density (30.51 mW cm$^{-2}$). This study not only advances the design of bifunctional electrocatalysts but also expands a universal synthesis paradigm for transition metal hydroxide-supported noble metal hybrids.

This work was supported by the National Key Research and Development Program of China (No. 2024YFA1211101 and 2024YFA1211102), the National Natural Science Foundation of China (Grant No. 52432004, U22A20141, U23A20575, and 52472183), and the Research Funding of Hangzhou International Innovation Institute of Beihang University (Grant No. 2024KQ102 and 2024KQ131).

## Conflicts of interest

There are no conflicts to declare.

## Data availability

The data supporting this article have been included as part of the supplementary information (SI). Supplementary information is available. See DOI: https://doi.org/10.1039/d5cc04360c.

## Notes and references

1 T. Jin, S. Shen, A. Xu, J. Pan, G. Zhou and W. Zhong, *Small*, 2025, **21**, 2500667.
2 Z. Yan, Z. Liu, G. Zhou, T. Jin, H. Zhang, L. Gu, T. Gao, S. Shen and W. Zhong, *Angew. Chem., Int. Ed.*, 2025, **64**, e202501964.
3 H. Yu, D. Liu, Z. Fu, S. Wang, X. Zuo, X. Feng and Y. Zhang, *Angew. Chem., Int. Ed.*, 2024, **63**, e202401272.
4 D. Liu, Z. Fu, S. Wang, X. Gong, T. You, H. Yu, Y. Jiang and Y. Zhang, *Angew. Chem., Int. Ed.*, 2025, **64**, e202425277.
5 M. Xie, Y. Lu, X. Xiao, D. Wu, B. Shao, H. Nian, C. Wu, W. Wang, J. Gu, S. Han, M. Gu and Q. Xu, *Adv. Funct. Mater.*, 2025, **35**, 2414537.

6 H. Seong, K. Min, G. Lee, K. Kwon and S.-H. Baeck, *Appl. Catal., B*, 2025, **362**, 124725.

7 P. Moni, S. Hyun, A. Vignesh and S. Shanmugam, *Chem. Commun.*, 2017, **53**, 7836–7839.

8 Q. Wang, Z. L. Zhao, Z. Zhang, T. Feng, R. Zhong, H. Xu, S. T. Pantelides and M. Gu, *Adv. Sci.*, 2020, **7**, 1901279.

9 Q. Xu, L. Zhang, L. Li, S. Zhang, Y. Zhou and G. Hu, *Adv. Funct. Mater.*, 2024, **35**, 2414379.

10 M. Niu, Q. Guan, W. Yuan, C. X. Guo, D. Cao, C. M. Li, L. Y. Zhang and X. S. Zhao, *Chem. Eng. J.*, 2025, **503**, 158465.

11 Y. Liu, J. Ma, S. Jia, C. Ma, P. Wu, L. Yang, L. Shen and G. Zhang, *Int. J. Hydrogen Energy*, 2025, **100**, 378–387.

12 M. Guo, X. Guan, Q. Meng, M.-L. Gao, Q. Li and H.-L. Jiang, *Angew. Chem., Int. Ed.*, 2024, **63**, e202410097.

13 J. Ye, M. Wu, B. Zhu, B. Cheng and J. Yu, *J. Hazard. Mater.*, 2024, **474**, 134672.

14 B. Fan, H. Wang, X. Han, Y. Deng and W. Hu, *Chem. Commun.*, 2022, **58**, 8254–8257.

15 S. Pan, H. Shi, Y. Yu, Y. Li, Y. Chen, C. Li, Y. Sun, Z. Yang and F. Luo, *Chem. Commun.*, 2024, **60**, 11778–11781.

16 C. Han, Y. Yuan, G. Chen, Z. Ye, Z. Guo and Y. Zhao, *ChemSusChem*, 2024, **17**, e202400812.

17 S. Shen, Q. Li, H. Zhang, D. Yang, J. Gong, L. Gu, T. Gao and W. Zhong, *Adv. Mater.*, 2025, **37**, 2500595.

18 M. Du, Y. Ji, Y. Li, S. Liu and J. Yan, *Adv. Funct. Mater.*, 2024, **34**, 2402776.

19 X. Zhao, H. Zheng, H. Sun, M. Chen, B. Wang, Q. Lu, B. Xiao, T. Zhou, D. Li, G. Qiu, J. Zhang, Y. Zhang, F. Liu, T. He, H. Pan, C. Wang and Q. Liu, *Nano Energy*, 2025, **142**, 111201.

20 Y. Zhong, Y. Zhang, J. Wang, H. Jin, S. Pan, S. Wang and Y. Chen, *Energy Environ. Sci.*, 2025, **18**, 991–1001.

21 J. Song, Y. Chen, H. Huang, J. Wang, S.-C. Huang, Y.-F. Liao, A. E. Fetohi, F. Hu, H.-Y. Chen, L. Li, X. Han, K. M. El-Khatib and S. Peng, *Adv. Sci.*, 2022, **9**, 2104522.

22 Y. Chen, H. Yao, F. Kong, H. Tian, G. Meng, S. Wang, X. Mao, X. Cui, X. Hou and J. Shi, *Appl. Catal., B*, 2021, **297**, 120474.

23 O. Ambriz-Peláez, J. Béjar, C. M. Ramos-Castillo, M. Guerra-Balcázar, L. Álvarez-Contreras and N. Arjona, *Appl. Surf. Sci.*, 2022, **601**, 154253.

24 N. Allwyn, S. Gokulnath and M. Sathish, *ACS Appl. Mater. Interfaces*, 2024, **16**, 20360–20374.

25 X. Hu, W. Tian, Z. Wu, X. Li, Y. Li and H. Wang, *J. Colloid Interface Sci.*, 2024, **672**, 610–617.

26 W.-H. Wang, C.-H. Han, W.-X. Hong, Y.-C. Chiu, I. H. Tseng, Y.-H. Chang, H. Pourzolfaghar and Y.-Y. Li, *J. Energy Storage*, 2024, **85**, 111058.

27 T. Aziz, A. Kumar, M. K. Awasthi, Y. P. Kharwar, I. Karajagi, V. Vishal, P. C. Ghosh, D. P. Dubal and A. Dutta, *ACS Appl. Energy Mater.*, 2024, **7**, 11297–11308.

28 X. Han, N. Li, J. S. Baik, P. Xiong, Y. Kang, Q. Dou, Q. Liu, J. Y. Lee, C. S. Kim and H. S. Park, *Adv. Funct. Mater.*, 2023, **33**, 2212233.